THE JOURNAL OF
PHYSICAL CHEMISTRY
LETTERS
A JOURNAL OF THE AMERICAN CHEMICAL SOCIETY

August 24, 2023
Volume 14
Number 33
pubs.acs.org/JPCL

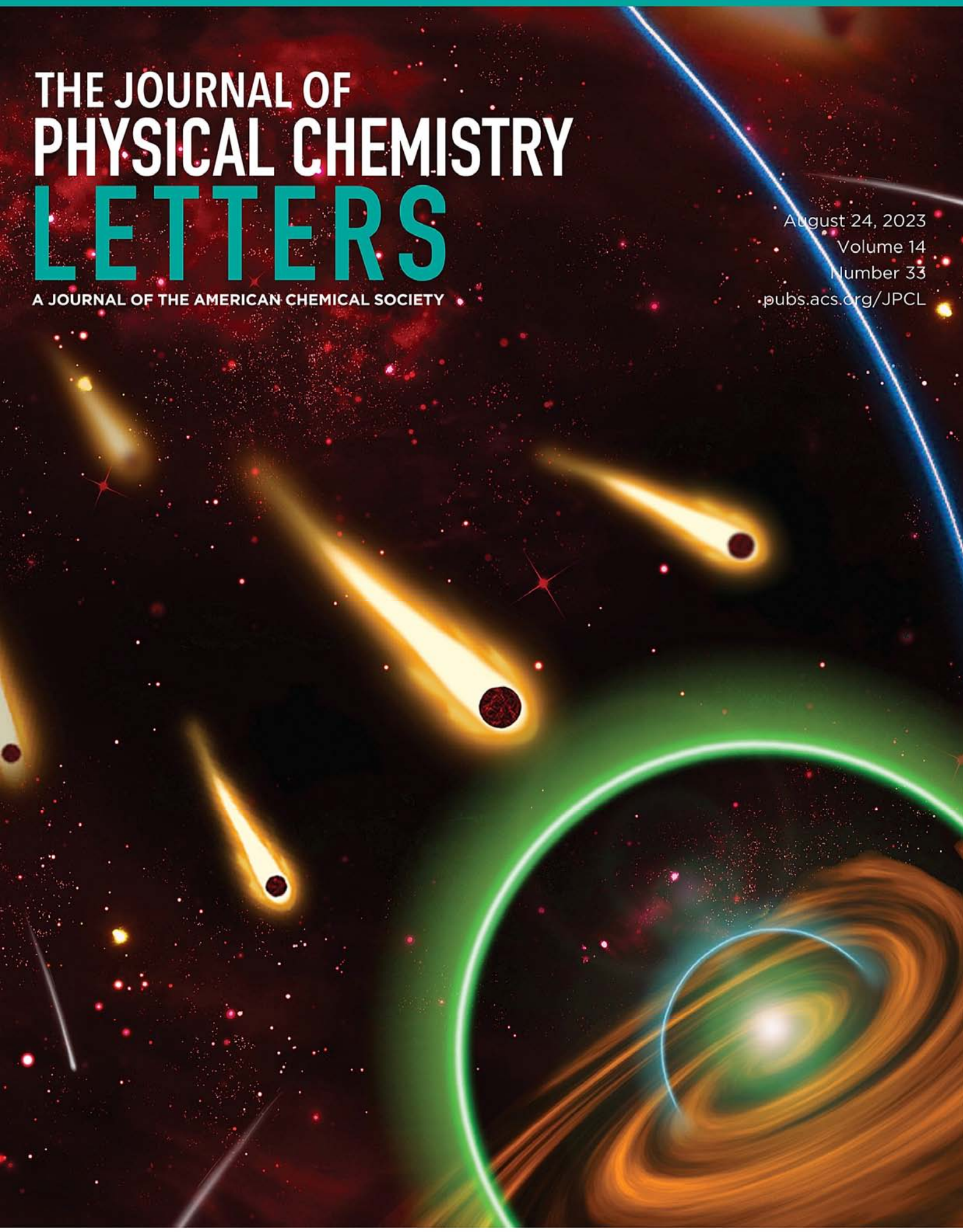

ACS Publications
Most Trusted. Most Cited. Most Read.

www.acs.org

THE JOURNAL OF PHYSICAL CHEMISTRY LETTERS
A JOURNAL OF THE AMERICAN CHEMICAL SOCIETY

pubs.acs.org/JPCL Letter

Improving the Five-Photon Absorption from Core–Shell Perovskite Nanocrystals

Xuanyu Zhang, Shuyu Xiao, Zhihang Guo, Baozhen Yuan, Xiongbin Wang, Samo Zhang, Yueqing Shi, Guichuan Xing, Tingchao He,* and Rui Chen*

Cite This: *J. Phys. Chem. Lett.* 2023, 14, 7581–7590 Read Online

ACCESS | Metrics & More | Article Recommendations | Supporting Information

ABSTRACT: It is necessary to improve the action cross section ($\eta \times \sigma_n$) of high-order multiphoton absorption (MPA) for fundamental research and practical applications. Herein, the core–shell $FAPbBr_3/CsPbBr_3$ nanocrystals (NCs) were constructed, and fluorescence induced by up to five-photon absorption was observed. The value of $\eta \times \sigma_5$ reaches 8.64×10^{-139} cm^{10} s^4 $photon^{-4}$ nm^{-3} at 2300 nm, which is nearly an order of magnitude bigger than that of the core-only NCs. It is found that the increased dielectric constant promotes modulation of MPA effects, addressing the electronic distortion in high-order nonlinear behaviors through the local field effect. Meanwhile, the quasi-type-II band alignment suppresses the biexciton Auger recombination, ensuring the stronger MPA induced fluorescence. In addition, the core–shell structure can not only reduce the defect density but also promote the nonradiative energy transfer though the antenna-like effect. This work provides a new avenue for the exploitation of high-performance multiphoton excited nanomaterials for future photonic integration.

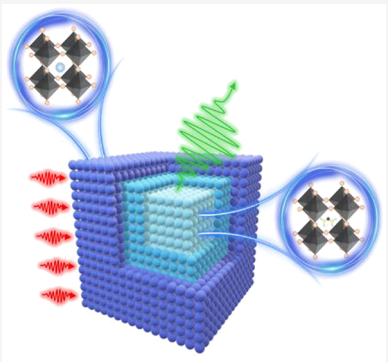

Multiphoton absorption (MPA) refers to a nonlinear optical (NLO) process in which electrons simultaneously absorb multiple monochromatic photons and transit from the ground state to the excited state. High energy photons are subsequently generated through radiative recombination. Compared with one-photon excitation, MPA possesses the characteristics of stronger spatial confinement, longer laser penetration depth, less biological damage, and Rayleigh scattering.[1−7] Thanks to this, MPA has shown great prospects in three-dimensional biomedical imaging, photodynamic therapy, optical power confinement, sensing, and optical data storage.[8−13] In the past few years, there has been an explosion of research on low-order MPA in materials.[14−18] However, reports of high-order MPA such as four-photon absorption (4PA) and five-photon absorption (5PA) are very rare. It is recognized that, in order to achieve high-order MPA induced fluorescence, materials with large action cross section ($\eta \times \sigma_n$) are needed, where η is the photoluminescence quantum yield (PLQY) and σ_n is the MPA cross section. The values of $\eta \times \sigma_{n\geq 4}$ in traditional semiconductor nanocrystals (NCs) and organic compounds are relatively small, so strong excitation is required to achieve MPA, which can easily damage the materials and greatly limit their practical application.

However, the emergence of perovskites reversed this situation. They have demonstrated amazing MPA properties, and the number of publications on this area has increased dramatically since 2016.[16,19−21] Subsequently, many studies have been conducted to improve the MPA of various perovskite NCs.[22−26] Unfortunately, most of the observed MPA enhancements are closely related to the size of the material. The MPA action cross section of the perovskite material itself has hardly improved, especially for the high-order MPA. At present, the core–shell structure reported by Sum et al. may be the only effective technical solution.[23] They fabricated core–shell $MAPbBr_3/(OA)_2PbBr_4$ (3D/2D) NCs, which increased the MPA action cross section by about 5 times per nm^3. However, the synthesis process of the core–shell NCs is complex. More importantly, selecting 2D perovskite as the shell can result in serious lattice mismatch. A large surface to volume ratio leads to more defect states and weak carrier transitions of 2D $(OA)_2PbBr_4$, making the enhancement of the $\eta \times \sigma_5$ far from reaching its limit.

In order to eliminate the above disadvantages, a 3D/3D core–shell structure formed through heterogeneous epitaxy may be a better solution to further improve the MPA property. Among various perovskite materials reported so far, $FAPbBr_3$ NCs with stronger emission and longer exciton lifetime[27] due to the large dielectric polarization effect and the spatial confinement of the surface electronic (or polaron) state[28] have been considered as a potential candidate for the core material. According to its ionic crystal structure, it is necessary for the shell to follow the same structure to the minimum boundary

Received: July 3, 2023
Accepted: July 31, 2023
Published: August 17, 2023

https://doi.org/10.1021/acs.jpclett.3c01809
J. Phys. Chem. Lett. 2023, 14, 7581−7590

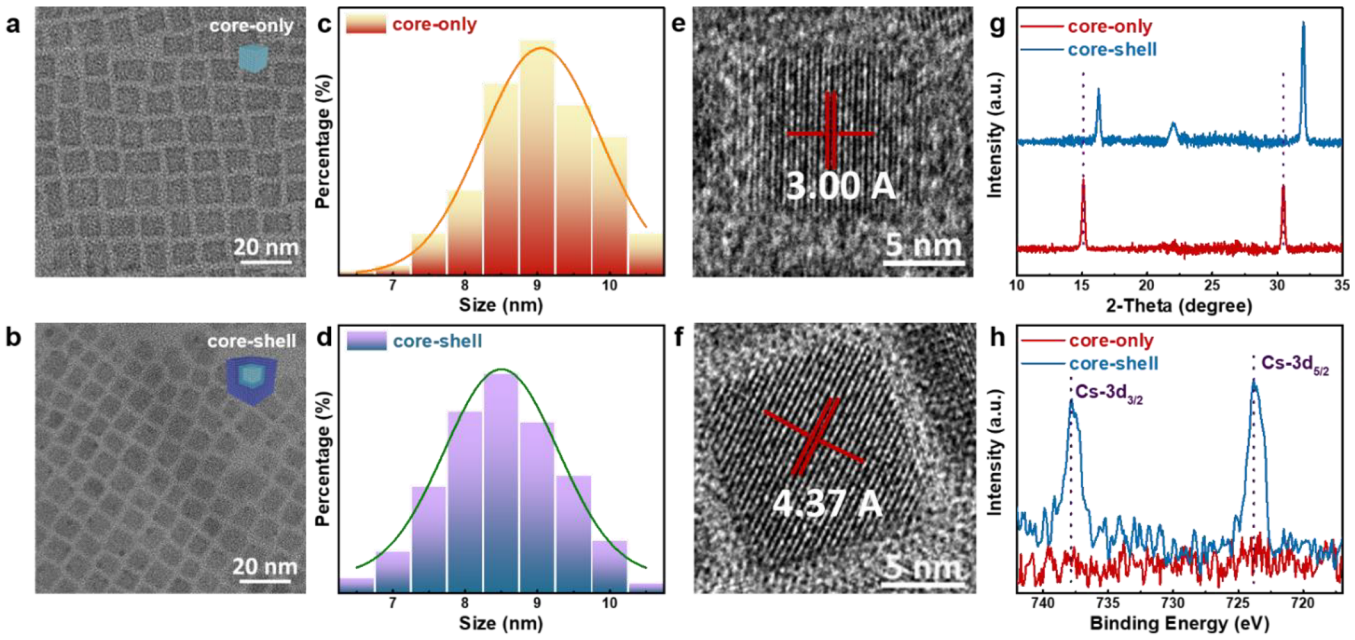

Figure 1. (a, b) TEM images of the core-only $FAPbBr_3$ and core−shell $FAPbBr_3/CsPbBr_3$ colloidal NCs, respectively. Inset: schematic of the colloidal NCs. (c, d) Size distribution of the samples in (a) and (b), respectively. (e, f) HRTEM images of the typical $FAPbBr_3$ and $FAPbBr_3/CsPbBr_3$ NCs, respectively. (g) XRD patterns of $FAPbBr_3$ and $FAPbBr_3/CsPbBr_3$ NCs. (h) XPS spectra of Cs 3d regions in $FAPbBr_3$ and $FAPbBr_3/CsPbBr_3$ NCs.

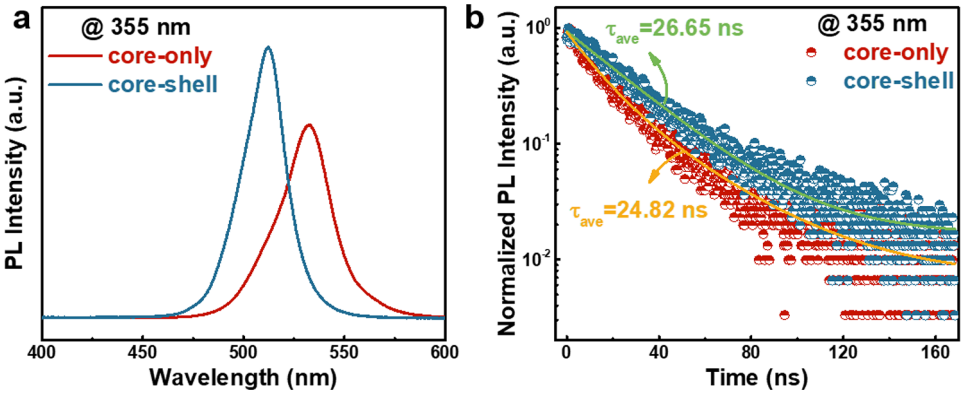

Figure 2. (a) One-photon PL spectra from the core-only $FAPbBr_3$ (red curve) and core−shell $FAPbBr_3/CsPbBr_3$ (blue curve) colloidal NCs at room temperature. (b) One-photon PL decay curves in the core-only $FAPbBr_3$ (red curve) and core−shell $FAPbBr_3/CsPbBr_3$ (blue curve) colloidal NCs at room temperature.

effect. Taking the lattice constant and band structure into consideration, $CsPbBr_3$ can be selected as the shell material. Therefore, in this work, the core−shell $FAPbBr_3/CsPbBr_3$ (3D/3D) colloidal NCs were fabricated, which showed a significant enhancement of the MPA action cross section. The 5PA action cross section was determined by the method of multiphoton absorption photoluminescence saturation (MPAPS), which was 8.64×10^{-139} cm^{10} s^4 $photon^{-4}$ nm^{-3} at 2300 nm. In addition, the underlying physical mechanisms for enhancing the NLO properties have been discussed in detail. This work on giant MPA enhancement in core−shell perovskite NCs is unprecedented, which opens up new prospects toward next-generation multiphoton applications.

The typical transmission electron microscopy (TEM) image presented in Figure 1a shows that the core-only $FAPbBr_3$ colloidal NCs have a cubic shape with an average size of around 9.0 nm. In general, the overgrowth of shell leads to an increase in the size of NCs. Considering that the NLO properties are greatly affected by the size of NCs, it is necessary to strictly control the growth conditions of core and shell to discuss the impact of the shell. As displayed in Figure 1b, the core−shell NCs maintain a cubic shape with well-defined edges and corners, and the average size is about 8.5 nm. The insets of Figure 1a,b show the schematic structures of the synthesized core-only and core−shell NCs, respectively. As shown in Figure 1e,f, the high-resolution transmission electron microscopy (HRTEM) images reveal that the crystal spacing of the core-only and core−shell NCs is about 3.00 and 4.37 Å, respectively, which indicates that strain is generated at the core−shell interfaces due to the lattice mismatch. This also confirms the successful overgrowth of $CsPbBr_3$ shell on the surface of $FAPbBr_3$ NCs.[29,30] Meanwhile, X-ray diffraction (XRD) was used to further investigate the structural characteristics of the two samples (Figure 1g). The core-only NCs show the primary diffraction peaks at 14.8°, 21.1°, and 29.8°, which are assigned to the (100), (110), and (200)

https://doi.org/10.1021/acs.jpclett.3c01809
J. Phys. Chem. Lett. 2023, 14, 7581−7590

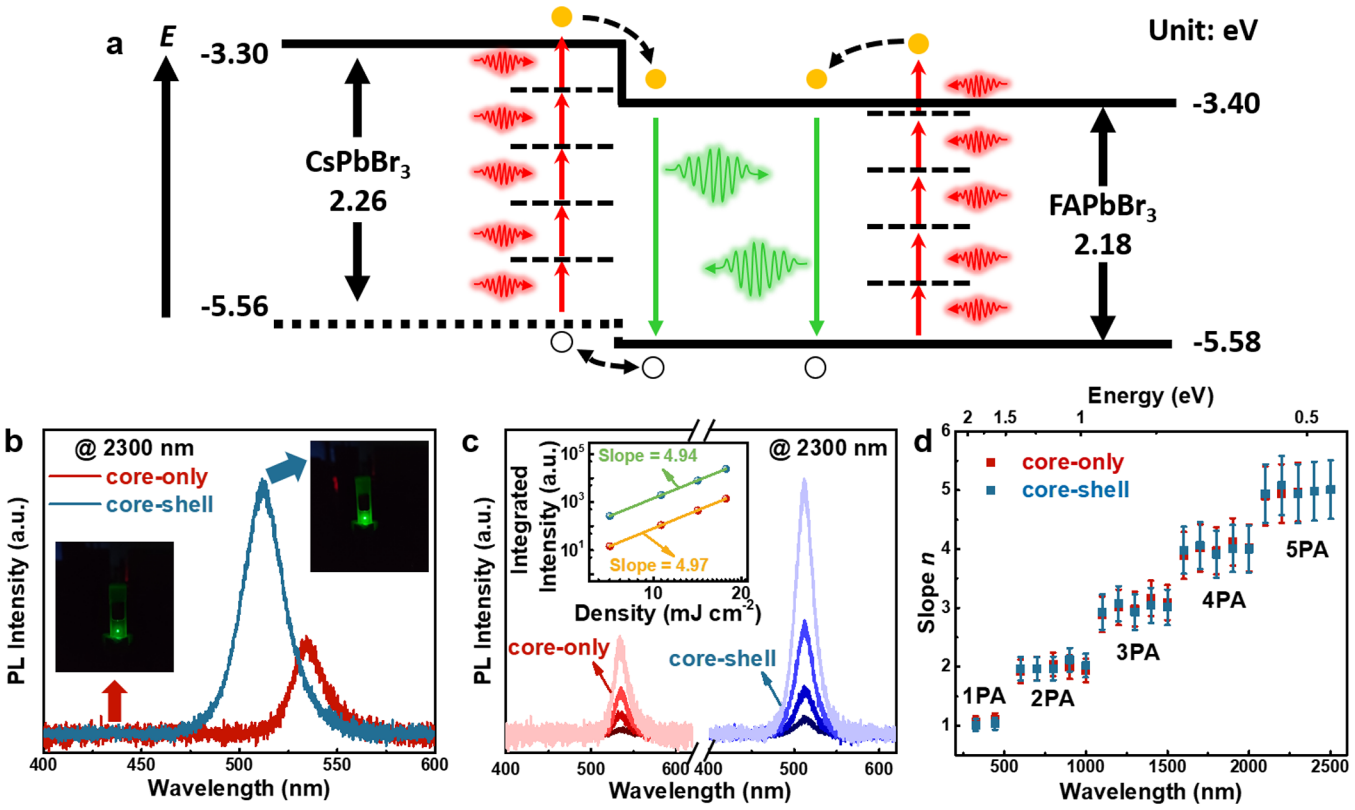

Figure 3. (a) Schematic illustration of the five-photon PL process in the core−shell $FAPbBr_3/CsPbBr_3$ colloidal NCs. (b) Five-photon PL spectra of the core-only $FAPbBr_3$ (red curve) and core−shell $FAPbBr_3/CsPbBr_3$ (blue curve) colloidal NCs at room temperature. Insets: images of the core-only (lower left) and core−shell (top right) NCs under 2300 nm femtosecond irradiation. (c) Five-photon PL spectra from the core-only $FAPbBr_3$ and core−shell $FAPbBr_3/CsPbBr_3$ colloidal NCs with femtosecond laser excitation at 2300 nm. Inset shows the quintic dependence on the excitation fluence of the spectrally integrated PL intensity. (d) Slope n plotted as a function of laser excitation wavelength (photon energy), where n is defined as the excitation fluence dependence of the multiphoton PL signal that is proportional to (excitation fluence)^n.

planes of cubic perovskite NCs.[31] While these diffraction peaks of the core−shell NCs shift toward higher angles, indicating the overgrowth of the $CsPbBr_3$ shell, no signal of alloyed perovskite NCs can be observed, which can be explained by the virtue of the Vegard's law.[32−34] Taking into account the ionic characteristics of $CsPbBr_3$ and $FAPbBr_3$, there may be a gradient alloy layer $FA_{1-x}Cs_xPbBr_3$ in the core−shell NCs, which may lead to a decrease in the defect density of states at the core−shell interface. Moreover, in contrast to the core-only NCs, the X-ray photoelectron spectroscopy (XPS) of the core−shell NCs presented two distinct peaks at 723.7 and 737.8 eV. These peaks were assigned to the binding energy of Cs, providing evidence of its incorporation into the lattice, as depicted in Figures 1h and S1. Therefore, it is suggested that a gradient alloy layer exists in $FA_{1-x}Cs_xPbBr_3$.

Figure 2a plots the photoluminescence (PL) from the core-only (red line) and core−shell (blue line) NCs under the excitation of 355 nm laser pulses. It can be seen clearly that the emission from the core-only NCs is located at 532.8 nm, while the PL of core−shell NCs is blue-shifted to 512.3 nm, which can be attributed to the decrease in effective size of the $FAPbBr_3$ core of the core−shell NCs. Meanwhile, the formation of the $FA_{1-x}Cs_xPbBr_3$ gradient alloy layer during the shell growth also results in the blueshift of emission. The PL decay curves of the core-only and core−shell NCs are presented in Figure 2b, and the average PL lifetimes deduced from the fitting are 24.82 and 26.65 ns, respectively. It can be found that the core−shell NCs possess stronger emission and longer lifetime under the same experimental conditions, which implies the effective passivation of nonradiative surface defects by the $CsPbBr_3$ shell.

The electronic structure of the core−shell $FAPbBr_3/CsPbBr_3$ NCs has been confirmed to be the quasi-type-II band alignment in our previous research based on the temperature-dependent PL measurement and theoretical calculation,[35] characterized by a partial spatial separation between the electron and hole wave functions. The values of conduction and valence band offsets in the core−shell NCs are 0.10 and 0.02 eV, respectively, which result in the confinement of electrons in the core region, while holes are delocalized into the entire core−shell region. The schematic energy band diagram and excitation process of the core−shell NCs is illustrated in Figure 3a. It is interesting to note that MPA induced emissions up to the order of 5 have been detected from the samples. Figure 3b shows the 5PA (that is, at 2300 nm wavelength) induced excitonic PL (around 512 and 532 nm) from the core-only (red line) and core−shell (blue line) NCs, respectively. The insets show the corresponding optical images under excitation. Figure 3c presents the power-dependent PL spectra for 5PA of the two samples with excitation density ranging from around 7.07 to 17.68 mJ cm^{-2}, and their quintic excitation fluence dependence is shown in the inset. A summary of the excitation wavelength dependence of the slopes (that is, orders of MPA process) for the core-only and core−shell NCs under excitation wavelengths from 600 to 2500 nm is plotted in Figure 3d, and the detailed spectra can

https://doi.org/10.1021/acs.jpclett.3c01809
J. Phys. Chem. Lett. 2023, 14, 7581−7590

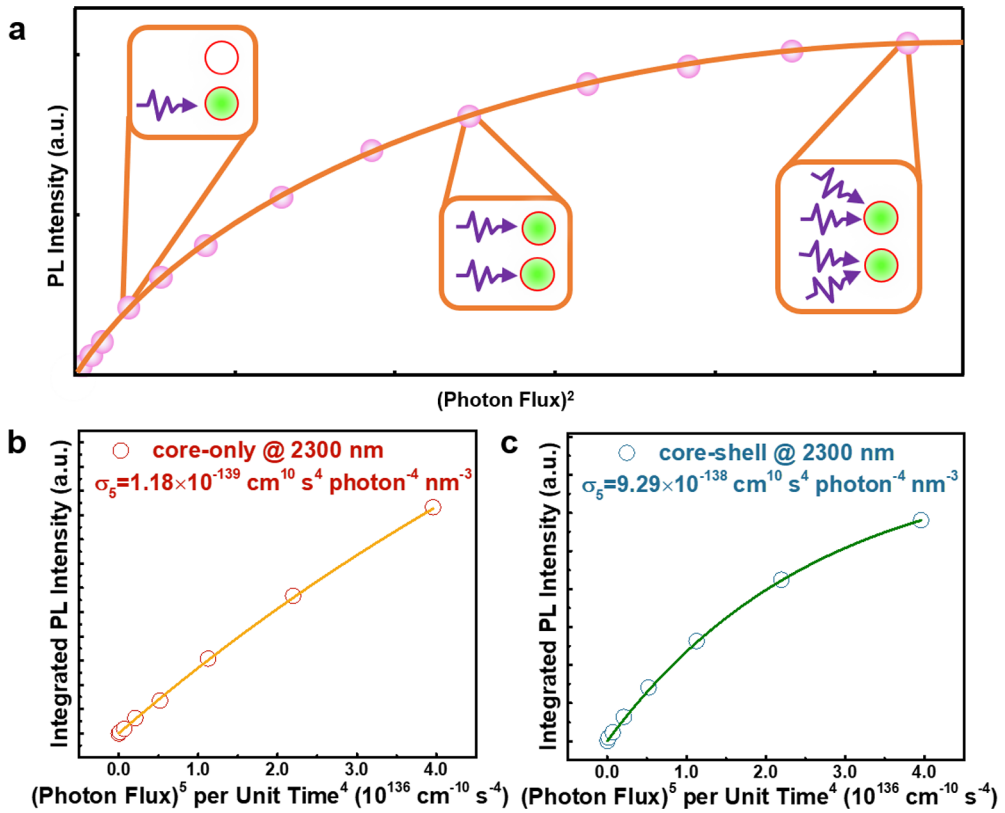

Figure 4. (a) Schematic diagram shows the mechanism of MPAPS. (b, c) MPAPS curves of the core-only $FAPbBr_3$ and core−shell $FAPbBr_3$/$CsPbBr_3$ colloidal NCs at 2300 nm, respectively.

be seen in Figures S2−S5. The slopes of the emission from the samples are around 2 in the wavelength range of 600−1000 nm, clearly indicating the 2PA process. With the increase of excitation wavelength to 1100−1500 nm, the slopes increase to around 3, revealing a switching of the excitation mechanism to 3PA. Similarly, when the excitation wavelength increases to the range of 1600−2000 nm, the 4PA process (with slopes around 4) dominates. Within the longer wavelength range of 2100−2500 nm, the slope is around 5, indicating that the 5PA process is dominant. It is worth noting that in the excitation wavelength range of 2400−2500 nm only emission from the core−shell NCs can be detected. The absence of the emission from the core-only NCs can be ascribed to the limited excitation power, or the signal is too weak to be detected. This implies that it is easier for the core−shell NCs to achieve a higher-order MPA process such as six-photon-induced PL. However, the excitation wavelength required for measurement cannot be achieved due to the limitation of the laser system.

The core−shell NCs exhibit stronger PL over the entire excitation wavelength range of 600 to 2500 nm. Therefore, it is necessary to compare the MPA action cross sections of the two samples to explore the physical mechanism of the enhancement. According to the definition of MPA action cross section, the first parameter that needs to be determined is the PLQY. Compared with the PLQY of 82% for the core-only NCs, the value for the core−shell NCs is improved up to 93%, further indicating effective passivation of nonradiative surface defects due to the shell epitaxy. The second parameter that needs to be determined is the MPA cross section of the two samples. In general, the Z-scan technique is the most common method to determine MPA, and it does work well for low-order MPA. Unfortunately, when it comes to high-order NLO behavior, the signal analysis and data processing become extremely complex. As shown in Figures S6 and S7, both the core-only and core−shell NCs exhibit narrow and sharp emission under both 2PA and 3PA. The signal of the core-only NCs can still be recorded for MPA up to the order of 5, as shown in Figures S8 and S9. A closer look at the emission from the core−shell NCs reveals a progressively wider shape of the curve compared to that of the core-only NCs. Moreover, the emission broadens more severely with the increase in excitation wavelength. Furthermore, it is worth noting that whether it is the core-only or core−shell NCs, with the increase of power density, their signals are undergoing extremely serious broadening, as displayed in Figure S10. This implies that the cascading MPA signal in the Z-scan was more obvious. Meanwhile, the inset in Figure S10 shows a smaller slope value derived from the power-dependent Z-scan for the core−shell NCs, which implies that the Z-scan technique fails to differentiate direct MPA and cascade MPA.[36] In this case, the MPA cross section obtained is not credible. The lack of reliable references for high-order ($n \geq 3$) MPA in multiphoton-excited PL[37] limits the applicability of this method.

Therefore, the effective MPAPS method proposed by Padilha et al. was used to evaluate the MPA cross section of the samples,[38] taking advantage of the fact that multiexciton species in NCs hardly emit, as depicted in Figure 4a. This new method does not rely on any specific properties of NCs, allowing an accurate comparative study of samples with different structures or exhibiting slow multicarrier dynamics. The results show that the MPAPS method can be adjusted to correctly obtain the MPA cross section for NCs with a slower Auger recombination rate. To test the reliability of the MPAPS method, the 2PA cross section of rhodamine 6G (R6G) was

https://doi.org/10.1021/acs.jpclett.3c01809
J. Phys. Chem. Lett. 2023, 14, 7581−7590

measured at 800 nm, and a result of ~3.11 × 10^{-49} cm^2 s^1 $photon^{-1}$ was obtained, which is basically consistent with the value reported in previous literature.[39,40]

For a given MPA, plotting time-integrated PL intensity as a function of (photon flux)^n per unit time^{n-1} results in a linear dependence at low excitation densities and reaches saturation at higher power densities as depicted in Figure 4a. The experimental data can be fitted by the following equation[38]

$$\mathrm{PL} = A\left[(1 - e^{-\langle N\rangle})\left(1 + \frac{\mathrm{QY_{XX}}}{\mathrm{QY_X}}\right) - \frac{\mathrm{QY_{XX}}}{\mathrm{QY_X}}(\langle N\rangle e^{-\langle N\rangle})\right] \quad (1)$$

where $\langle N\rangle$ is the average number of the excited exciton per NC and QY_X and QY_{XX} are the single exciton and biexciton quantum yield, respectively. A is a proportionality constant, which depends on the value of QY_X, the solution concentration of NCs, and the emission collection efficiency of the measurement system. Accordingly, the MPA action cross sections of the core-only and core−shell NCs can be obtained at excitation wavelengths of 800, 1300, 2000, and 2300 nm (Figures S11 and 4). The results are summarized in Table 1.

Table 1. Comparison of the MPA Action Cross Sections of the Core-Only $FAPbBr_3$ and Core−Shell $FAPbBr_3/CsPbBr_3$ Colloidal NCs

	excitation source	core-only	core−shell
PLQY	xenon lamp	82%	93%
$\eta\sigma_1$ (10^{-17} cm^2 s^0 $photon^0$ nm^{-3})	400 nm, 100 fs, 1 kHz	0.27	2.67
$\eta\sigma_2$ (10^{-47} cm^4 s^1 $photon^{-1}$ nm^{-3})	800 nm, 100 fs, 1 kHz	0.28	2.30
$\eta\sigma_3$ (10^{-77} cm^6 s^2 $photon^{-2}$ nm^{-3})	1300 nm, 100 fs, 1 kHz	0.63	5.50
$\eta\sigma_4$ (10^{-107} cm^8 s^3 $photon^{-3}$ nm^{-3})	2000 nm, 100 fs, 1 kHz	1.28	11.30
$\eta\sigma_5$ (10^{-139} cm^{10} s^4 $photon^{-4}$ nm^{-3})	2300 nm, 100 fs, 1 kHz	0.97	8.64

Specifically, in all cases, the value of $\eta \times \sigma_n$ per nm^3 of the core−shell NCs is 8−9 times that of the core-only NCs, which is larger than the previously reported value.[23] The ratio of the action cross section between the core−shell and the core-only NCs is listed in Table 2, in which the 1PA cross section was

Table 2. Ratio of the Core−Shell NCs over the Core-Only NCs for Different Multiphoton Absorption Processes

n-photon absorption process	ratio of the core−shell over the core-only
1	7.98
2	8.21
3	8.79
4	8.83
5	8.91

determined by transient absorption spectroscopy (Figure S12). It can be found that the value increases with the increase of the order of multiphoton absorption, which indicates the optical response of the core-only NCs becomes less sensitive under higher-order excitation. Moreover, in order to better highlight the enhancement effect of the core-shell structure on the MPA action cross-section, the comparsion of the obtain values in this work to the results reported in a variety of perovskite materials was shown in Table 3. Obviously, the values of MPA action cross-section in the core-only $FAPbBr_3$ NCs are almost the smallest in all the listed materials. However, through the construction of the core-shell structure, it can be significantly enhanced, making it stand out from many similar materials. Therefore, it is necessary to analyze in detail the reasons for this enhancement in order to expand the application of perovksite nanomaterials in multiphonics.

For the physical mechanism that significantly enhances the performance of NLO, there is no doubt that the first reason to consider is the polarization P under an applied external field E can be expressed by[41]

$$P = \varepsilon_0\chi_{ab}E_b + \varepsilon_0\chi_{abc}E_bE_c + \varepsilon_0\chi_{abcd}E_bE_cE_d + \cdots \quad (2)$$

where ε_0 is the vacuum dielectric constant, E is the applied external field, χ_{ab} is the secondary rank tensor, and χ_{abc} and χ_{abcd} are the higher order tensors. The relationship of dielectric constant ε and the polarization can be described by

$$\varepsilon = \varepsilon_0 + \frac{P}{E} \quad (3)$$

It can be easily found that the nonlinearity of polarization is positively related to that of dielectric constant. It is clear that the essence of the susceptibility lies in the effective dielectric constant of the core−shell NCs, which also leads to dielectric confinement (local field effect). Notably, the core−shell NCs in this work possess a cubic lattice. Therefore, when the NLO response is considered, it is completely different from the traditional spherical shape. ε of the core−shell NCs is calculated by[42]

$$\varepsilon = \frac{3\varepsilon_c(\varepsilon_c + 2\varepsilon_s)}{\varepsilon_c + 2\varepsilon_s - (\varepsilon_c - \varepsilon_s)[L/(L + 2d)]} - 2\varepsilon_s \quad (4)$$

where ε_c and ε_s are the dielectric constant of the core and shell. Obviously, the polarization of the cubic core−shell NCs depends not only on the difference between the core and shell materials but also on the size of the core−shell NCs, which is not as simple as previously reported.[23] Since the sizes of the core-only and core−shell NCs are almost the same, the only effect on the nonlinear polarization is the difference in the dielectric constant. In the case of the same size, the greater the difference between the dielectric constant of the core and the shell, the greater is the dielectric constant of the core−shell structure, which in turn, exhibits a stronger NLO response. As far as we know, the dielectric constant difference of 21.6 between the core and the shell in this work is the largest reported so far.[43,44] To be specific, the relationship between the polarization intensity P of n-photon absorption and the $(2n - 1)$ order nonlinear susceptibility $\chi^{(2n-1)}$ conforms to

$$\chi^{(2n-1)} = \frac{e^{(n+1)}}{\varepsilon m^n d^{(n+2)}\omega^{2n}} \quad (5)$$

where e is the charge of an electron, m is the mass of an electron, d is the lattice spacing, and ω is the frequency of the applied external field E. Therefore, the nonlinear susceptibility of the core-only and core−shell NCs can be quantitatively analyzed. For example, the third-order nonlinear susceptibility $\chi^{(3)}$ of the two NCs was calculated as 1.05 × 10^{-11} and 1.70 × 10^{-11} esu, respectively. Similarly, for higher-order nonlinear susceptibility, the law is the same. More importantly, this gap of the nonlinear susceptibility between the core-only and core−shell NCs becomes larger at higher n (higher-order

https://doi.org/10.1021/acs.jpclett.3c01809
J. Phys. Chem. Lett. 2023, 14, 7581−7590

Table 3. Comparison of the MPA Action Cross Sections of the Core-Only $FAPbBr_3$ and Core−Shell $FAPbBr_3/CsPbBr_3$ Colloidal NCs with the Reported Values from Similar Materials

materials	$\eta\sigma_1$ (10^{-17} cm^2 s^0 $photon^0$ nm^{-3})	$\eta\sigma_2$ (10^{-47} cm^4 s^1 $photon^{-1}$ nm^{-3})	$\eta\sigma_3$ (10^{-77} cm^6 s^2 $photon^{-2}$ nm^{-3})	$\eta\sigma_4$ (10^{-107} cm^8 s^3 $photon^{-3}$ nm^{-3})	$\eta\sigma_5$ (10^{-139} cm^{10} s^4 $photon^{-4}$ nm^{-3})	refs
$CsPbBr_3$		17.83	10.43	9.47	8.92	23
$MAPbBr_3$		7.13	3.70	4.11	3.29	23
$MAPbBr_3$/$(OA)_2PbBr_4$		37.00	22.00	24.00	20.00	23
$CsPbBr_{2.7}I_{0.3}$		0.84	0.56	0.36	0.33	24
ZJU-28⊃$MAPbBr_3$		1.73	1.05	0.20	3.98	25
$(IA)_2(MA)_2Pb_3Br_{10}$		1.60×10^{-19}	7.79×10^{-18}	2.49×10^{-16}	4.68×10^{-14}	26
$CsPbCl_3$	7.60	0.08	0.02			58
$CsPbCl_{1.5}Br_{1.5}$	14.7	0.21	0.17			58
$CsPbBr_3$	25.80	0.24	0.19			58
$CsPbBr_{1.5}I_{1.5}$	44.79	0.87	2.49			58
$CsPbI_3$	101.37	5.82	30.47			58
$FAPbBr_3$	0.27	0.28	0.63	1.28	0.97	this work
$FAPbBr_3/CsPbBr_3$	2.67	2.30	5.50	11.30	8.64	this work

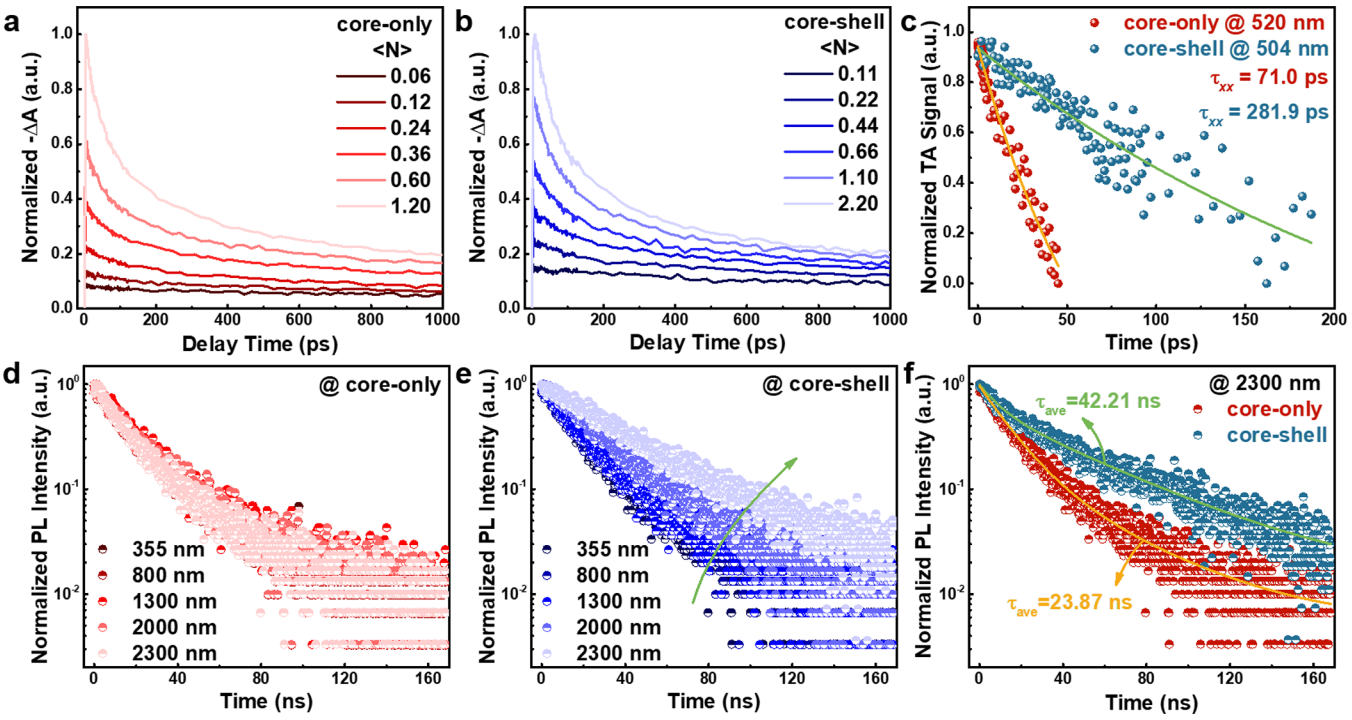

Figure 5. (a, b) TA kinetics of the core-only $FAPbBr_3$ and core−shell $FAPbBr_3/CsPbBr_3$ NCs with different particle numbers ⟨N⟩ excited at 355 nm. (c) Biexciton recombination kinetics for the core-only $FAPbBr_3$ (red points) and core−shell $FAPbBr_3/CsPbBr_3$ (blue points) NCs and their fits to single-exponential decay functions (lines). (d, e) One- and multiphoton-excited PL decay curves in the core-only $FAPbBr_3$ and core−shell $FAPbBr_3/CsPbBr_3$ colloidal NCs at room temperature. (f) Five-photon PL decay and corresponding fitting curves of (d) and (e) at 2300 nm.

nonlinearity), just as the results show in Table 2. Meanwhile, it is generally recognized that the shape of the nanoparticles possesses a serious impact on the NLO behavior, and it has been confirmed that susceptibility losses in the cube are the lowest.[45] All of the above factors led to the excellent NLO response of the core−shell $FAPbBr_3/CsPbBr_3$ NCs. In addition, the local field due to the intrinsic piezoelectric polarization charges present at the $FAPbBr_3/CsPbBr_3$ interface is typical in strained heterostructure due to both the high piezoelectric constants and the elastic strain induced by the lattice mismatch between the $FAPbBr_3$ core and the $CsPbBr_3$ shell.[46] Under the influence of this internal electric field, both the energy level and wave function of the electrons are changed, which in turn leads to changes in the optical matrix elements and shielding of the electric field by photogenerated electron−hole pairs. The enhanced internal electric field further benefits the photoinduced screening, which may be another plausible origin of the enhanced NLO property.

Next, Auger recombination is known to be the predominant nonradiative recombination mechanism for NCs, especially under high excitation density, which is harmful to the occurrence of MPA induced fluorescence. It has been confirmed that the electronic structure of the core−shell $FAPbBr_3/CsPbBr_3$ NCs is quasi-type-II band alignment, which can suppress Auger recombination and reduce the exciton−exciton annihilation.[47−51] The Auger lifetimes of the core-only

https://doi.org/10.1021/acs.jpclett.3c01809
J. Phys. Chem. Lett. 2023, 14, 7581−7590

and core−shell NCs are determined to discuss the Auger process. The pump-fluence-dependent ground state bleaching (GSB) decay processes of the core-only and core−shell NCs were detected at the carrier density n_0 ranging from 3.23×10^{16} to 1.62×10^{18} cm^{-3} and from 1.79×10^{17} to 8.95×10^{18} cm^{-3}, as illustrated in Figure 5a,b, respectively. According to the procedure discussed in previous literature,[52] one should normalize the GSB decay curves at a long decay time (3 ns) and then subtract from the GSB curve at the lowest fluence pumping. It is noted that the extracted kinetics can be fitted by a single-exponential decay, and the values of the biexciton lifetime (τ_{XX}) are determined to be 71.0 and 281.9 ps for the core-only and core−shell NCs, respectively (Figure 5c). The biexciton decay process is dominated by the biexciton Auger recombination and radiative recombination. The biexciton radiative recombination is considered to be a quarter of the single-exciton radiative lifetime (τ_{XR}).[53] Obviously, the value of τ_{XX} is much shorter than a quarter of that of τ_{XR}, which emphasizes the biexciton Auger recombination mechanism. The quasi-type-II band alignment of the core−shell NCs leads to longer biexciton radiative recombination lifetime, which contributes to the emission. Therefore, the suppression of Auger recombination in core−shell NCs with a quasi-type-II electronic structure may also be responsible for this enhancement of MPA cross section.

Then, the effective passivation of nonradiative surface defects by the growth of $CsPbBr_3$ shell can be verified from the comparison of PL intensity, PL lifetime, and PLQY. Due to the growth of the shell, this passivation directly increases the probability of multiphoton transitions. In addition, the disappearance of the PL negative thermal quenching, as shown in Figure S13, supports this conclusion. At the same time, the good spectral overlap between the core absorption and the shell emission, as well as the intimate proximity between the core and shell, result in nonradiative Förster-type energy transfer from the shell to the core through an antenna-like effect. The photon energy can be absorbed by both the core and shells of NCs, and the $CsPbBr_3$ shell is used as a photon capture "antenna" to transfer the absorbed energy to the core, thereby effectively enhancing the overall MPA cross section of the NCs. Figure 5d,e presents the decay curves of one-photon-excited and multiphoton-excited time-resolved PL (TRPL) for the core-only and core−shell NCs, respectively. The PL decay curves under one- and multiphoton excitation from the core-only NCs are nearly constant, indicating excitation from the virtual state to the same lowest excited state. In contrast, the increased PL lifetimes from one- and multiphoton excitation from the core−shell NCs demonstrate the existence of the antenna-like effect; that is, the transfer of nonradiative energy from the shell to the core enhances the PL from the $FAPbBr_3$ NC core, and the longer multiphoton excited PL lifetime compared to the one-photon excited PL lifetime in the core−shell NCs also suggests that this nonradiative energy transfer channel contributes more to the emission from the core material. Notably, the variation of PL lifetimes of the core−shell NCs with excitation wavelength could be attributed to the strong laser field effects[54,55] (something similar to Stark effects), which may make it difficult to recombine radiatively, and therefore, there is a longer PL lifetime. Whatever, the increased PL lifetime of the core−shell NCs under 2300 nm excitation in Figure 5f proves the existence of an antenna-like effect,[56] which is beneficial to the MPA induced fluorescence.

Based on the discussion above, it can be concluded that an interplay of various factors arising from the effective surface passivation, the nonradiative energy transfer from the shell to the core through an antenna-like effect, the local field effect, the photoinduced screening of the internal field, the suppression of Auger recombination, or its combination gives rise to the giant enhancement of the MPA cross section of the core−shell NCs. Thanks to the core−shell structure with quasi-type-II band alignment, the optical properties of the material can be well modified. It is worth noting that, among the currently common perovskites, $FAPbBr_3$ NCs possess the smallest MPA cross section. The MPA cross section of core−shell perovskite NCs is expected to continue to increase if suitable shells can be found in the future, with $MAPbBr_3$ or $CsPbBr_3$ as core, which has a huge MPA cross section. These methods are universal and can provide reference for other material systems.

In conclusion, our findings indicate that the construction of a core−shell structure provides surprising enhancement in the 5PA action cross section. The value of MPA action cross section in $FAPbBr_3$ colloidal NCs can be enhanced by a factor of 8−9, reaching up to 10^{-139} cm^{10} s^4 $photon^{-4}$ nm^{-3} at 2300 nm by endowing this core−shell structure. Meanwhile, the relationship between the NLO behavior and the effective dielectric constant (local field effect and the resulting photoinduced screening) is elaborated in detail and is much more complex than previously reported. However, the formation of the core−shell structure is bound to lead to an increase in polarization. Moreover, the quasi-type-II band alignment of the core−shell structure suppressing Auger recombination is beneficial to MPA emission. In addition, the overgrowth of $CsPbBr_3$ shell effectively passivates the surface defects and promotes the antenna-like effect, which may be another plausible origin for the enhanced $\eta \times \sigma_n$. This work provides a new strategy for developing next-generation multiphoton imaging applications with unparalleled imaging depth, sensitivity, and resolution.

EXPERIMENTAL SECTION

Synthesis of Perovskite NCs. The core-only $FAPbBr_3$ and core−shell $FAPbBr_3/CsPbBr_3$ colloidal NCs were synthesized according to the method reported previously.[57] All reagents were purchased and used without further purification, including FA-acetate (Sigma-Aldrich), $Pb(CH_3COO)_2{\cdot}3H_2O$ (Sinopharm Chemical Reagent Co., Ltd., ≥99.5%), octadecene (ODE, Sigma-Aldrich, 90%), OA (Sigma-Aldrich, 90%), OAmBr (Xi'an Polymer Light Technology Crop), toluene (Sinopharm Chemical Reagent Co., Ltd., ≥99.5%), $PbBr_2$ (Sigma-Aldrich, 90%), Cs_2CO_3 (Sigma-Aldrich), and OLA (Sigma-Aldrich, 90%). Briefly, FA-acetate (0.078 g, 0.75 mmol), $Pb(CH_3COO)_2{\cdot}3H_2O$ (0.076 g, 0.2 mmol), OA (2 mL, vacuum-dried at 120 °C), and ODE (8 mL, vacuum-dried at 120 °C) were loaded into a 100 mL flask and dried for 30 min under vacuum at 50 °C. The mixture was heated to 130 °C under N_2 atmosphere, and OAmBr (0.21 g, 0.6 mmol) in toluene (2 mL) was injected. After 10 s, the reaction mixture was cooled on an ice−water bath. The green solution of $FAPbBr_3$ NCs was collected and stored at 4 °C.

For the synthesis of core−shell $FAPbBr_3/CsPbBr_3$ colloidal NCs, $PbBr_2$ (0.1101 g, 0.3 mmol) and Cs_2CO_3 (0.0326 g, 0.1 mmol) were loaded into a 100 mL flask. Then, dried OA (1 mL), ODE (5 mL), and OLA (0.5 mL) and as-synthesized $FAPbBr_3$ colloidal NCs (12 mL) were added. The mixture was

https://doi.org/10.1021/acs.jpclett.3c01809
J. Phys. Chem. Lett. 2023, 14, 7581−7590

heated to 80 °C for 20 min under N_2 atmosphere and then cooled on an ice bath. Finally, the solution was centrifuged to remove undispersed residues and aggregated perovskite NCs. The core−shell $FAPbBr_3/CsPbBr_3$ colloidal NCs were dispersed in hexane and stored in the dark at 4 °C. It is known that the nonlinear optical properties of the materials depend on their size. Therefore, fabrication has been controlled to ensure a similar size of the materials for effective comparison.

Purification. As-prepared crude solutions of the core-only $FAPbBr_3$ and core−shell $FAPbBr_3/CsPbBr_3$ colloidal NCs were loaded into centrifuge tubes, and a certain volume of ethyl acetate was added (the volume ratio of crude solution and ethyl acetate was kept at 1:3); then, the mixtures were centrifuged at 7000 rpm for 5 min. The precipitate was then redissolved in *n*-hexane and centrifuged for 1 min at 5000 rpm. Afterward, the supernatant was collected and stored at 4 °C. Finally, after washing twice or three times, the purified colloidal NC solution could be obtained.

Structure Characterization. Samples for TEM measurements were prepared by dropping a relatively dilute solution of colloidal NCs onto carbon-coated 200 mesh copper grids. Conventional TEM images were acquired by a FEI Talos F200X microscope equipped with a thermionic gun under an acceleration voltage of 200 kV. The current of the 1 nm electron beam at this voltage is 1.5 nA, and the resolution is 0.12 nm.

Optical Characterization. The PLQY was measured by Hamamatsu Quantaurus-QY with model No. C11347. All emissions were dispersed by a monochromator (Andor SR-750-D1-R) and detected using a Newton charge-coupled device (model No. DU920P-BU). Femtosecond laser pulses (Coherent Astrella ultrafast Ti:sapphire laser with OperA Solo, pulse width of 100 fs, and repetition rate of 1 kHz) were selected as the excitation source for power-dependent PL measurements as well as the TRPL experiments. For the decay measurement, the signal was dispersed by a 320 mm monochromator (iHR320 from Horiba, Ltd.) combined with suitable filters and detected based on the time-correlated single photon counting technique. The pumping laser was focused via a 40× objective, and the laser spot was controlled by manipulating the collimation of the pumping beam. According to the grating of 600 g mm^{-1}, 26 μm pixel size of the camera, and 100 μm slit width, the spectral resolution of the optical measurement was determined to be around 0.24 nm. Transient absorption measurements were conducted using an ExciPro XL Femtosecond Transient Absorption Pump−Probe Spectrometer (CDP systems). The solution of perovskite colloidal NCs was filled in a quartz cuvette with a path length of 1 mm and a volume of 0.35 mL and was pumped with a femtosecond 355 nm laser pulse generated from an optical parametric amplifier. The probe pulses ranging from 380 to 800 nm were derived from the fundamental 800 nm laser pulses with a small portion (~5 μJ) of a 2 mm thick CaF_2 plate.

■ ASSOCIATED CONTENT

Supporting Information

The Supporting Information is available free of charge at https://pubs.acs.org/doi/10.1021/acs.jpclett.3c01809.

Additional details including MPA induced PL, Z-scan, MPA cross-section fitting, and temperature-dependent PL results (PDF)

■ AUTHOR INFORMATION

Corresponding Authors

Tingchao He − *College of Physics and Optoelectronic Engineering, Shenzhen University, Shenzhen 518060, China;* orcid.org/0000-0003-1040-0596; Email: tche@szu.edu.cn

Rui Chen − *Department of Electrical and Electronic Engineering, Southern University of Science and Technology, Shenzhen 518055, China;* orcid.org/0000-0002-0445-7847; Email: chenr@sustech.edu.cn

Authors

Xuanyu Zhang − *Department of Electrical and Electronic Engineering, Southern University of Science and Technology, Shenzhen 518055, China*

Shuyu Xiao − *College of Physics and Optoelectronic Engineering, Shenzhen University, Shenzhen 518060, China*

Zhihang Guo − *College of Physics and Optoelectronic Engineering, Shenzhen University, Shenzhen 518060, China*

Baozhen Yuan − *Department of Electrical and Electronic Engineering, Southern University of Science and Technology, Shenzhen 518055, China*

Xiongbin Wang − *Department of Electrical and Electronic Engineering, Southern University of Science and Technology, Shenzhen 518055, China*

Samo Zhang − *Department of Electrical and Electronic Engineering, Southern University of Science and Technology, Shenzhen 518055, China*

Yueqing Shi − *Department of Electrical and Electronic Engineering, Southern University of Science and Technology, Shenzhen 518055, China*

Guichuan Xing − *The Institute of Applied Physics and Materials Engineering, University of Macau, Taipa, Macau 519000, China;* orcid.org/0000-0003-2769-8659

Complete contact information is available at: https://pubs.acs.org/10.1021/acs.jpclett.3c01809

Notes

The authors declare no competing financial interest.

■ ACKNOWLEDGMENTS

This work is supported by the National Natural Science Foundation of China (62174079) and Science, Technology and Innovation Commission of Shenzhen Municipality (Project Nos. JCYJ20220530113015035, JCYJ20210324120204011, JCYJ20190808121211510, and KQTD20150717103136556).

■ REFERENCES

(1) Denk, W.; Strickler, J. H.; Webb, W. W. Two-photon laser scanning fluorescence microscopy. *Science* **1990**, *248*, 73−76.

(2) Helmchen, F.; Denk, W. Deep tissue two-photon microscopy. *Nat. Methods* **2005**, *2*, 932−940.

(3) Palczewska, G.; Maeda, T.; Imanishi, Y.; Sun, W.; Chen, Y.; Williams, D. R.; Piston, D. W.; Maeda, A.; Palczewski, K. Noninvasive multiphoton fluorescence microscopy resolves retinol and retinal condensation products in mouse eyes. *Nat. Methods* **2010**, *16*, 1444−1449.

(4) Horton, N. G.; Wang, K.; Kobat, D.; Clark, C. G.; Wise, F. W.; Schaffer, C. B.; Xu, C. In vivo three-photon microscopy of subcortical structures within an intact mouse brain. *Nat. Photonics* **2013**, *7*, 205−209.

(5) Yong, K.-T.; Qian, J.; Roy, I.; Lee, H. H.; Bergey, E. J.; Tramposch, K. M.; He, S.; Swihart, M. T.; Maitra, A.; Prasad, P. N.

Quantum rod bioconjugates as targeted probes for confocal and two-photon fluorescence imaging of cancer cells. *Nano Lett.* **2007**, *7*, 761−765.
(6) Zhang, C.; Zhang, F.; Qian, S.; Kumar, N.; Hahm, J.-i.; Xu, J. Multiphoton absorption induced amplified spontaneous emission from biocatalyst-synthesized ZnO nanorods. *Appl. Phys. Lett.* **2008**, *92*, 233116.
(7) Hoover, E. E.; Squier, J. A. Advances in multiphoton microscopy technology. *Nat. Photonics* **2013**, *7*, 93−101.
(8) Maruo, S.; Nakamura, O.; Kawata, S. Three-dimensional microfabrication with two-photon-absorbed photopolymerization. *Opt. Lett.* **1997**, *22*, 132−134.
(9) Bhawalkar, J.; Kumar, N.; Zhao, C.-F.; Prasad, P. Two-photon photodynamic therapy. *J. Clin. Laser Med. Sur.* **1997**, *15*, 201−204.
(10) Pawlicki, M.; Collins, H. A.; Denning, R. G.; Anderson, H. L. Two-photon absorption and the design of two-photon dyes. *Angew. Chem., Int. Ed.* **2009**, *48*, 3244−3266.
(11) Ehrlich, J.; Wu, X.; Lee, I.-Y.; Hu, Z.-Y.; Röckel, H.; Marder, S.; Perry, J. Two-photon absorption and broadband optical limiting with bis-donor stilbenes. *Opt. Lett.* **1997**, *22*, 1843−1845.
(12) Pond, S. J.; Tsutsumi, O.; Rumi, M.; Kwon, O.; Zojer, E.; Brédas, J.-L.; Marder, S. R.; Perry, J. W. Metal-ion sensing fluorophores with large two-photon absorption cross sections: Aza-crown ether substituted donor-acceptor-donor distyrylbenzenes. *J. Am. Chem. Soc.* **2004**, *126*, 9291−9306.
(13) Cumpston, B. H.; Ananthavel, S. P.; Barlow, S.; Dyer, D. L.; Ehrlich, J. E.; Erskine, L. L.; Heikal, A. A.; Kuebler, S. M.; Lee, I.-Y. S.; McCord-Maughon, D. Two-photon polymerization initiators for three-dimensional optical data storage and microfabrication. *Nature* **1999**, *398*, 51−54.
(14) Agarwal, G.; Harshawardhan, W. Inhibition and enhancement of two photon absorption. *Phys. Rev. Lett.* **1996**, *77*, 1039−1042.
(15) He, G. S.; Xu, G. C.; Prasad, P. N.; Reinhardt, B. A.; Bhatt, J. C.; Dillard, A. G. Two-photon absorption and optical-limiting properties of novel organic compounds. *Opt. Lett.* **1995**, *20*, 435−437.
(16) Walters, G.; Sutherland, B. R.; Hoogland, S.; Shi, D.; Comin, R.; Sellan, D. P.; Bakr, O. M.; Sargent, E. H. Two-photon absorption in organometallic bromide perovskites. *ACS Nano* **2015**, *9*, 9340−9346.
(17) Gao, Y.; Wang, S.; Huang, C.; Yi, N.; Wang, K.; Xiao, S.; Song, Q. Room temperature three-photon pumped $CH_3NH_3PbBr_3$ perovskite microlasers. *Sci. Rep.* **2017**, *7*, 45391.
(18) He, J.; Qu, Y.; Li, H.; Mi, J.; Ji, W. Three-photon absorption in ZnO and ZnS crystals. *Opt. Express* **2005**, *13*, 9235−9247.
(19) Wang, Y.; Li, X.; Zhao, X.; Xiao, L.; Zeng, H.; Sun, H. Nonlinear absorption and low-threshold multiphoton pumped stimulated emission from all-inorganic perovskite nanocrystals. *Nano Lett.* **2016**, *16*, 448−453.
(20) Yamada, Y.; Yamada, T.; Phuong, L. Q.; Maruyama, N.; Nishimura, H.; Wakamiya, A.; Murata, Y.; Kanemitsu, Y. Dynamic optical properties of $CH_3NH_3PbI_3$ single crystals as revealed by one- and two-photon excited photoluminescence measurements. *J. Am. Chem. Soc.* **2015**, *137*, 10456−10459.
(21) Hirori, H.; Xia, P.; Shinohara, Y.; Otobe, T.; Sanari, Y.; Tahara, H.; Ishii, N.; Itatani, J.; Ishikawa, K. L.; Aharen, T.; Ozaki, M.; Wakamiya, A.; Kanemitsu, Y. High-order harmonic generation from hybrid organic-inorganic perovskite thin films. *APL Mater.* **2019**, *7*, No. 041107.
(22) Nakagawa, K.; Hirori, H.; Sanari, Y.; Sekiguchi, F.; Sato, R.; Saruyama, M.; Teranishi, T.; Kanemitsu, Y. Interference effects in high-order harmonics from colloidal perovskite nanocrystals excited by an elliptically polarized laser. *Phys. Rev. Mater.* **2021**, *5*, No. 016001.
(23) Chen, W.; Bhaumik, S.; Veldhuis, S. A.; Xing, G.; Xu, Q.; Grätzel, M.; Mhaisalkar, S.; Mathews, N.; Sum, T. C. Giant five-photon absorption from multidimensional core-shell halide perovskite colloidal nanocrystals. *Nat. Commun.* **2017**, *8*, 15198.
(24) Li, J.; Zhao, F.; Xiao, S.; Cheng, J.; Qiu, X.; Lin, X.; Chen, R.; He, T. Giant two-to five-photon absorption in $CsPbBr_{2.7}I_{0.3}$ two-dimensional nanoplatelets. *Opt. Lett.* **2019**, *44*, 3873−3876.
(25) He, H.; Cui, Y.; Li, B.; Wang, B.; Jin, C.; Yu, J.; Yao, L.; Yang, Y.; Chen, B.; Qian, G. Confinement of perovskite-QDs within a single MOF crystal for significantly enhanced multiphoton excited luminescence. *Adv. Mater.* **2019**, *31*, 1806897.
(26) Li, M.; Xu, Y.; Han, S.; Xu, J.; Xie, Z.; Liu, Y.; Xu, Z.; Hong, M.; Luo, J.; Sun, Z. Giant and broadband multiphoton absorption nonlinearities of a 2D organometallic perovskite ferroelectric. *Adv. Mater.* **2020**, *32*, 2002972.
(27) Zhumekenov, A. A.; Saidaminov, M. I.; Haque, M. A.; Alarousu, E.; Sarmah, S. P.; Murali, B.; Dursun, I.; Miao, X.-H.; Abdelhady, A. L.; Wu, T. Formamidinium lead halide perovskite crystals with unprecedented long carrier dynamics and diffusion length. *ACS Energy Lett.* **2016**, *1*, 32−37.
(28) Jesper Jacobsson, T.; Correa-Baena, J.-P.; Pazoki, M.; Saliba, M.; Schenk, K.; Gratzel, M.; Hagfeldt, A. Exploration of the compositional space for mixed lead halogen perovskites for high efficiency solar cells. *Energy Environ. Sci.* **2016**, *9*, 1706−1724.
(29) Gao, Y.; Liu, Y.; Zhang, F.; Bao, X.; Xu, Z.; Bai, X.; Lu, M.; Wu, Y.; Wu, Z.; Zhang, Y. High-performance perovskite light-emitting diodes enabled by passivating defect and constructing dual energy-transfer pathway through functional perovskite nanocrystals. *Adv. Mater.* **2022**, *34*, 2207445.
(30) Cottingham, P.; Brutchey, R. L. On the crystal structure of colloidally prepared $CsPbBr_3$ quantum dots. *Chem. Commun.* **2016**, *52*, 5246−5249.
(31) Arora, N.; Dar, M. I.; Hezam, M.; Tress, W.; Jacopin, G.; Moehl, T.; Gao, P.; Aldwayyan, A. S.; Deveaud, B.; Grätzel, M. Photovoltaic and amplified spontaneous emission studies of high-quality formamidinium lead bromide perovskite films. *Adv. Funct. Mater.* **2016**, *26*, 2846−2854.
(32) Zhang, C.; Wang, S.; Li, X.; Yuan, M.; Turyanska, L.; Yang, X. Core/shell perovskite nanocrystals: Synthesis of highly efficient and environmentally stable $FAPbBr_3/CsPbBr_3$ for LED applications. *Adv. Funct. Mater.* **2020**, *30*, 1910582.
(33) Sutton, R. J.; Eperon, G. E.; Miranda, L.; Parrott, E. S.; Kamino, B. A.; Patel, J. B.; Hörantner, M. T.; Johnston, M. B.; Haghighirad, A. A.; Moore, D. T. Bandgap-tunable cesium lead halide perovskites with high thermal stability for efficient solar cells. *Adv. Energy Mater.* **2016**, *6*, 1502458.
(34) Sutton, R. J.; Eperon, G. E.; Miranda, L.; Parrott, E. S.; Kamino, B. A.; Patel, J. B.; Hörantner, M. T.; Johnston, M. B.; Haghighirad, A. A.; Moore, D. T. Bandgap-tunable cesium lead halide perovskites with high thermal stability for efficient solar cells. *Adv. Energy Mater.* **2016**, *6*, 1502458.
(35) Zhang, X.; Guo, Z.; Li, R.; Yu, J.; Yuan, B.; Chen, B.; He, T.; Chen, R. Quasi-type II core-shell perovskite nanocrystals for improved structural stability and optical gain. *ACS Appl. Mater. Interfaces* **2021**, *13*, 58170−58178.
(36) Webster, S.; Fu, J.; Padilha, L. A.; Przhonska, O. V.; Hagan, D. J.; Van Stryland, E. W.; Bondar, M. V.; Slominsky, Y. L.; Kachkovski, A. D. Comparison of nonlinear absorption in three similar dyes: Polymethine, squaraine and tetraone. *Chem. Phys.* **2008**, *348*, 143−151.
(37) Xu, C.; Webb, W. W. Measurement of two-photon excitation cross sections of molecular fluorophores with data from 690 to 1050 nm. *J. Opt. Soc. Am. B* **1996**, *13*, 481−491.
(38) Alo, A.; Barros, L. W.; Nagamine, G.; Vieira, L. B.; Chang, J. H.; Jeong, B. G.; Bae, W. K.; Padilha, L. A. Simple yet effective method to determine multiphoton absorption cross section of colloidal semiconductor nanocrystals. *ACS Photonics* **2020**, *7*, 1806−1812.
(39) Albota, M. A.; Xu, C.; Webb, W. W. Two-photon fluorescence excitation cross sections of biomolecular probes from 690 to 960 nm. *Appl. Opt.* **1998**, *37*, 7352−7356.
(40) Eggeling, C.; Volkmer, A.; Seidel, C. A. Molecular photobleaching kinetics of rhodamine 6G by one- and two-photon induced confocal fluorescence microscopy. *ChemPhysChem* **2005**, *6*, 791−804.

https://doi.org/10.1021/acs.jpclett.3c01809
J. Phys. Chem. Lett. 2023, 14, 7581−7590

(41) Wu, L.; Wang, X.; Gong, H.; Hao, Y.; Shen, Z.; Li, L. Core-satellite $BaTiO_3$@$SrTiO_3$ assemblies for a local compositionally graded relaxor ferroelectric capacitor with enhanced energy storage density and high energy efficiency. *J. Mater. Chem. C* **2015**, *3*, 750−758.
(42) Emelyanov, A. Y.; Pertsev, N. A.; Hoffmann-Eifert, S.; Böttger, U.; Waser, R. Grain-boundary effect on the curie-weiss law of ferroelectric ceramics and polycrystalline thin films: calculation by the method of effective medium. *J. Electroceram.* **2002**, *9*, 5−16.
(43) Govinda, S.; Kore, B. P.; Swain, D.; Hossain, A.; De, C.; Row, T. N. G.; Sarma, D. Critical comparison of $FAPbX_3$ and $MAPbX_3$ (X = Br and Cl): How do they differ? *J. Phys. Chem. C* **2018**, *122*, 13758−13766.
(44) Svirskas, Š.; Balčiūnas, S.; Šimėnas, M.; Usevičius, G.; Kinka, M.; Velička, M.; Kubicki, D.; Castillo, M. E.; Karabanov, A.; Shvartsman, V. V. Phase transitions, screening and dielectric response of $CsPbBr_3$. *J. Mater. Chem. A* **2020**, *8*, 14015−14022.
(45) Vasilakaki, M.; Binns, C.; Trohidou, K. N. Susceptibility losses in heating of magnetic core/shell nanoparticles for hyperthermia: a Monte Carlo study of shape and size effects. *Nanoscale* **2015**, *7*, 7753−7762.
(46) Morello, G.; Della Sala, F.; Carbone, L.; Manna, L.; Maruccio, G.; Cingolani, R.; De Giorgi, M. Intrinsic optical nonlinearity in colloidal seeded grown CdSe/CdS nanostructures: Photoinduced screening of the internal electric field. *Phys. Rev. B* **2008**, *78*, 195313.
(47) Zegrya, G. G.; Andreev, A. D. Mechanism of suppression of Auger recombination processes in type-II heterostructures. *Appl. Phys. Lett.* **1995**, *67*, 2681−2683.
(48) Mohseni, H.; Litvinov, V.; Razeghi, M. Interface-induced suppression of the Auger recombination in type-II InAs/GaSb superlattices. *Phys. Rev. B* **1998**, *58*, 15378.
(49) García-Santamaría, F.; Chen, Y.; Vela, J.; Schaller, R. D.; Hollingsworth, J. A.; Klimov, V. I. Suppressed auger recombination in "giant" nanocrystals boosts optical gain performance. *Nano Lett.* **2009**, *9*, 3482−3488.
(50) Park, Y.-S.; Bae, W. K.; Pietryga, J. M.; Klimov, V. I. Auger recombination of biexcitons and negative and positive trions in individual quantum dots. *ACS Nano* **2014**, *8*, 7288−7296.
(51) Rabouw, F. T.; Lunnemann, P.; van Dijk-Moes, R. J. A.; Frimmer, M.; Pietra, F.; Koenderink, A. F.; Vanmaekelbergh, D. Reduced Auger recombination in single CdSe/CdS nanorods by one-dimensional electron delocalization. *Nano Lett.* **2013**, *13*, 4884−4892.
(52) Castaneda, J. A.; Nagamine, G.; Yassitepe, E.; Bonato, L. G.; Voznyy, O.; Hoogland, S.; Nogueira, A. F.; Sargent, E. H.; Cruz, C. H. B.; Padilha, L. A. Efficient biexciton interaction in perovskite quantum dots under weak and strong confinement. *ACS Nano* **2016**, *10*, 8603−8609.
(53) Klimov, V. I. Multicarrier interactions in semiconductor nanocrystals in relation to the phenomena of Auger recombination and carrier multiplication. *Matter Phys.* **2014**, *5*, 285−316.
(54) Guo, C.; Li, M.; Nibarger, J. P.; Gibson, G. N. Single and double ionization of diatomic molecules in strong laser fields. *Phys. Rev. A* **1998**, *58*, R4271.
(55) Villeneuve, D. M.; Ivanov, M. Yu.; Corkum, P. B. Enhanced ionization of diatomic molecules in strong laser fields: A classical model. *Phys. Rev. A* **1996**, *54*, 736.
(56) Xing, G.; Chakrabortty, S.; Chou, K. L.; Mishra, N.; Huan, C. H. A.; Chan, Y.; Sum, T. C. Enhanced tunability of the multiphoton absorption cross-section in seeded CdSe/CdS nanorod heterostructures. *Appl. Phys. Lett.* **2010**, *97*, No. 061112.
(57) Protesescu, L.; Yakunin, S.; Bodnarchuk, M. I.; Bertolotti, F.; Masciocchi, N.; Guagliardi, A.; Kovalenko, M. V. Monodisperse formamidinium lead bromide nanocrystals with bright and stable green photoluminescence. *J. Am. Chem. Soc.* **2016**, *138*, 14202−14205.
(58) Pramanik, A.; Gates, K.; Gao, Y.; Begum, S.; Ray, P. C. Several orders-of-magnitude enhancement of multiphoton absorption property for $CsPbX_3$ perovskite quantum dots by manipulating halide stoichiometry. *J. Phys. Chem. C* **2019**, *123*, 5150−5156.

https://doi.org/10.1021/acs.jpclett.3c01809
J. Phys. Chem. Lett. 2023, 14, 7581−7590